Waveform Parsimonious Refraction Interferometry

Yicheng Zhou, *Student Member, IEEE*, and Sherif M. Hanafy

***Abstract*— A physics-based approach called waveform parsimonious refraction interferometry (WPRI), which interpolates head or refraction waveform, is introduced in this work. WPRI yields a significant advantage in exploration and engineering applications, as it mitigates the excessive time and labor cost in 2-D field acquisitions that require dense receivers and shots while improving coverage in refraction seismic imaging processes. Our proposed method generates the virtual seismic refraction waveform, which involves kinematic and dynamic information with near-perfect accuracy for near-surface seismic waveform inversion and migration. To achieve this, we record data from two shot locations situated at opposite ends of the seismic profile, as well as a handful of near-offset traces along the profile. The virtual head or refraction wavefield is then determined through the convolution and cross correlation of the recorded wavefields with the objective of eliminating common wavepath. Furthermore, we introduce a source wavelet deconvolution step to correct dynamic discrepancies present in the virtual waveform. By implementing this type of technique, we are able to produce virtual seismic data that are highly accurate and can be effectively employed in near-surface seismic imaging applications.**

***Index Terms*— Interferometry, inversion, migration, waveform.**

I. Introduction

THE significance of near-surface seismic imaging has been recognized to eliminate shallow, intricate geological effects in complex geological structure cases [1], [2]. Refraction survey has been proven to be a valuable tool in providing border convergence for velocity estimations [3] in the near-surface zone. Traditional near-surface seismic imaging methodologies rely on travel-time information and can be broken down into two primary components: tomography and migration [4]. These techniques are vital for characterizing the subsurface and are essential for conducting successful near-surface seismic imaging projects. The two primary components of traditional near-surface seismic imaging methodologies involve the utilization of refraction travel-time information to construct a subsurface velocity model [5], [6], [7] and the mapping of recorded travel-time information to the appropriate location [8], [9] under the ground. However, ray-based velocity estimation methods are susceptible to wavefront healing phenomena [10] and multipath issues. These two problems restrict the effectiveness of our method in scenarios where high-frequency assumptions [11], [12] are not satisfied or the anomaly size is considerably larger than the dominant wavelength of the source wavelet, which is common in complex geological environments. As a result, these methods are limited in their ability to accurately account for more complex velocity structures and may not provide optimal results in certain industry scenarios.

To address the limitations of ray-based velocity estimation methods, a notable wave-equation-based technique has been proposed [13], [14], [15] and referred to as full waveform inversion (FWI). For highly nonlinear and poor convergence problems in FWI, a time window of early arrivals has been applied and named as early arrival waveform inversion (EWI) [16], [17], [18]. It is not necessary to use waveform information as the input in this type of technology, and skeletonized data, such as refraction wavefield travel-time information, can also be utilized as input information in the wave-equation-based methodology to generate a starting velocity model [19] for subsequent waveform inversion processes and ultimately build to the construction of a more accurate subsurface velocity model. In addition, another reflectivity calculation method termed refraction wavefield migration [20], which involves the reconstruction of virtual reflection waveforms via reciprocal shots to map reflectivity, has been proposed. This innovative technology applies seismic interferometry to eliminate the common raypaths of two refraction wave events and convert them into virtual reflection gathers and then employs prestack depth migration to image the subsurface interface related to the refractor. This method is a variant of the interferometric reflection migration method, which utilizes data from surface and vertical seismic profiling (VSP) to generate high-resolution images of the subsurface structure [21], [22], [23].

In exploration seismology applications, seismic data are typically acquired by placing shots and geophones at fixed intervals along a 2-D acquisition line. To reduce both recording cost and acquisition time for travel-time tomography applications, the parsimonious refraction interferometry (PRI) technology is proposed [24]. This innovative approach calculates the summation of two postcritical travel times associated with the same refractor of the first and last shots, then subtracting the reciprocal travel time from the first and last shots and subtracting the reciprocal travel time from the first shot to the last geophone in order to obtain the virtual travel time. For near-offset traces that record direct events and do not honor the PRI principle assumption, several shot gathers are selected and direct arrivals are interpolated between them. This approach effectively yields $O(N^2)$ refraction travel times from $2N$ travel times obtained via two reciprocal shot gathers at both ends of the recording line and some infilled shot gathers [24], [25], where N is the number of geophones in the acquisition line. The resulting virtual refraction travel times

Manuscript received 12 March 2023; revised 9 August 2023 and 13 September 2023; accepted 4 October 2023. Date of publication 12 October 2023; date of current version 6 November 2023. This work was supported by the King Fahd University of Petroleum and Mineral (KFUPM). *(Corresponding author: Sherif M. Hanafy.)*

The authors are with the College of Petroleum Engineering and Geoscience, King Fahd University of Petroleum and Mineral, Dhahran 31261, Saudi Arabia (e-mail: yichenggeo@gmail.com; sherif.geo@gmail.com).

Digital Object Identifier 10.1109/TGRS.2023.3324134

provide border ray coverage, greater ray density, and enhanced model resolution in travel-time tomography. Furthermore, due to its significant reduction in acquisition time, the virtual travel time generated by PRI can be utilized to generate real-time subsurface snapshots [26], [27]. However, it is worth noting that the PRI methodology is not suitable for far offset and strong gradient velocity models that are related to diving wave mode because its raypath will not overlap and thus cannot be canceled out and the corresponding sources may not be on the stationary position. Finally, it is important to highlight that PRI can also be applied to surface waves [28].

In this article, we extend PRI technology into the waveform field [29] and name it as waveform PRI (WPRI), which will enhance the coverage of waveform imaging. This new procedure involves a combination of convolution and cross correlation techniques [30], [31] to generate virtual traces and source wavelet deconvolution [32] to eliminate extra source wavelets in the final result. Similar to the PRI method, WPRI is unable to interpolate diving waves and direct waves that do not conform to the refraction wavefield propagation. The underlying principle of WPRI is the reciprocity property in acoustic media which the reciprocal waveforms are identical in either kinematic or dynamic characteristics. However, in practical applications, the differences between the reciprocal traces will be aroused due to some factors, such as acquisition geometry configuration, background noises, and environment conditions [33]. To solve this problem, we propose a waveform reciprocity redatum procedure, which ensures that the reciprocity property is maintained prior to applying WPRI. Through the innovative application of these techniques, WPRI offers significant potential for improving the accuracy and efficiency of waveform imaging in near-surface seismic exploration and other geophysical applications.

Section II presents the theoretical foundations of our proposed methodology, including the waveform redatum procedure, the procedure to generate virtual shot gathers, and source wavelet deconvolution for dynamic character correction. Section III is divided into two parts. The first part focuses on presenting the results of our proposed method on synthetic data, where we utilized multiple input shot gathers to generate waveforms that were subsequently employed in EWI and refraction wavefield migration techniques to produce near-surface seismic images. As our proposed WPRI methodology can produce refraction waveforms with highly accurate kinematic and dynamic information, the results of EWI and refraction wavefield migration for both true and virtual refraction waveforms are very similar. The second part is testing the proposed method on a field dataset recorded along Aqaba fault, Eastern, Saudi Arabia. In this application, the seismic imaging results obtained using both the true and virtual data indicate the presence of an obvious fault, which is in accordance with the results of geological surveys. In both synthetic and field numerical data examples, we conduct a quantitative histogram of difference values in EWI and refraction wavefield migration to demonstrate WPRI's validity. Section IV provides a discussion of the limitations of our proposed methodology, while Section V gives further perspectives and recommendations for future research.

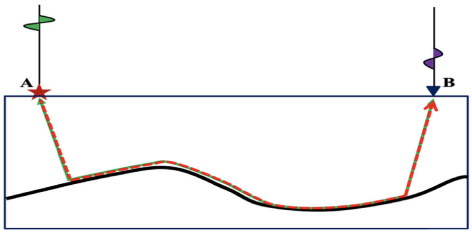

Fig. 1. Red dashed and green solid lines indicate the propagation direction of wavefield from A to B and from B to A, respectively. According to the reciprocity theorem, the arrival times from A to B and from B to A should be the same, however, in real data they may not.

II. Theory

A. Waveform Reciprocity Redatum

While there are some minor differences between the acoustic and elastic reciprocity properties, these variations do not result in any significant distortion in the far-field refraction wavefield which our research honors. The far-field reciprocity property [34] of Green's function ensures that the source and receiver can be interchanged, meaning that the two reciprocal traces activated by a source at point A to a receiver at point B should exhibit similar waveform characteristics as those generated by a source at point B to a receiver at point A. However, this reciprocity property may not always be true for real data due to some various environmental factors. A schematic example of this phenomenon is shown in Fig. 1, where the reciprocal traces exhibit different travel times and waveform characteristics. In practical applications, the reciprocity theorem should be obeyed before inversion and migration; otherwise, we should apply preprocess approaches to guarantee that the reciprocity theorem is satisfied.

In order to ensure that the waveform from two reciprocal traces possesses consistent kinematic and dynamic information, we recommend implementing a reciprocity redatum procedure before applying our proposed method. The following procedure outlines the steps required to achieve this objective.

1) Compare a reciprocal pair of the first and last common shot gathers (CSGs).
2) Use cross correlation operation to calculate the time lag (τ) between both traces [see (1) and Fig. 2(a)].
3) Shift both reciprocal traces (2) to align them, as shown in Fig. 2(b).
4) Replace both reciprocal traces by an average (3) of the shifted traces from step 3 [see (4)]. This will satisfy the reciprocity theorem, hence correcting the dynamic information as shown in Fig. 2(c)

$$d^{\text{corr}} = \text{corr}[d(A|B), d(B|A)] \tag{1}$$

$$d^1(A|B) = \text{shift}\left[d(A|B), \frac{\tau}{2}\right]$$

$$d^1(B|A) = \text{shift}\left[d(B|A), \frac{\tau}{2}\right] \tag{2}$$

$$d^{\text{Average}} = \frac{d^1(A|B) + d^1(B|A)}{2} \tag{3}$$

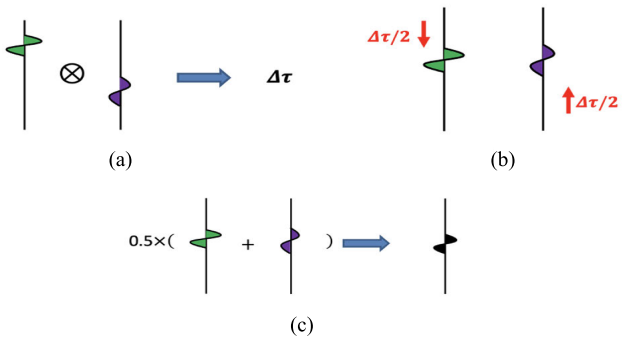

Fig. 2. To fix the kinematic and dynamic information of the reciprocal traces, (a) cross-correlate the reciprocal traces, (b) apply the kinematic correction by shifting the traces up/down, and (c) apply the dynamic correction by taking the average of both reciprocal traces.

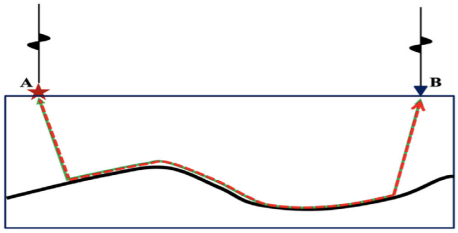

Fig. 3. Seismograms after kinematic and dynamic corrections.

$$d^2(A|B) = d^{\text{Average}}$$
$$d^2(B|A) = d^{\text{Average}}. \tag{4}$$

In the above context, $d(A|B)$ and $d(B|A)$ represent the recorded seismic data prior to the waveform redatum process, while $d^1(A|B)$ and $d^1(B|A)$ correspond to the reciprocal seismograms that result from kinematic correction. The travel-time lag τ is calculated based on the cross correlation between $d(A|B)$ and $d(B|A)$ [19]. Then, the average waveform is obtained by averaging the waveform after kinematic correction. In cases where there are significant differences between the reciprocal waveforms after kinematic correction, the average value is used to replace both of them to ensure that the reciprocal waveforms have the same dynamic information. As a result, $d^2(A|B)$ and $d^2(B|A)$ denote the waveforms after both kinematic and dynamic corrections and exhibit the same kinematic and dynamic characteristics, as shown in Fig. 3.

B. Convolution and Cross Correlation

Fig. 4(a) shows a two-layer medium containing an irregular refractor, along with a 2-D survey that has been deployed on surface. The acquisition geometry for this survey includes two reciprocal sources, A and D (represented by red solid stars) situated at the two edges of the acquisition line, as well as two receivers, B (indicated by an empty red star) and C (represented by a solid blue triangle), that have been selected between points A and D. To ensure that the received events correspond to refractions rather than directs, the offsets AC and DB have been selected to be larger than the crossover offset and should be guaranteed as the postcritical distance.

Green's function, which depicts the essential characteristics of the propagation path from point A to C, from point D to B, from point A to D, and from point B to C, is denoted as $G(A, \tau_{\mathbf{AC}}|C)$, $G(B, \tau_{BD}|D)$, $G(A, \tau_{\mathbf{AD}}|D)$, and

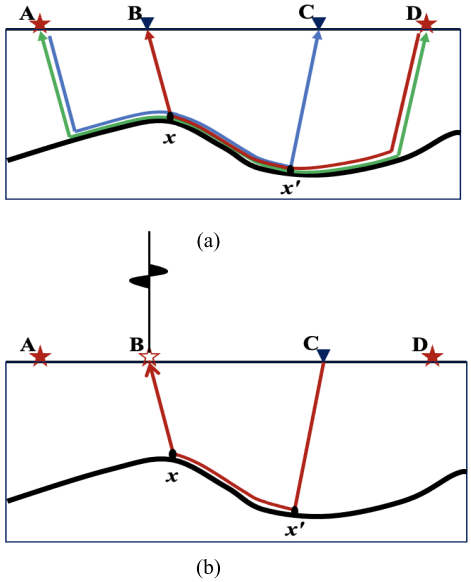

Fig. 4. WPRI method for a two-layer model, where the lower layer has a faster seismic velocity than the upper layer. (a) Green line represented the propagation direction associated with the wavefield, which activated from A and received by D. The blue line indicates the wavefield from A to C. The brown one is the wavefield from D to B. (b) Red path of the calculated wavefield through the convolution and cross correlation operations from B to C. The virtual data are also indicated above the model.

$G(B, \tau_{\mathbf{BC}}|C)$ [35]. These functions are graphically shown in Fig. 5(a)–(c). In the frequency domain, they are written as $e^{i(\omega\tau_{AC})}$, $e^{i(\omega\tau_{\mathbf{DB}})}$, $e^{i(\omega\tau_{\mathbf{AD}})}$, and $e^{i(\omega\tau_{\mathbf{BC}})}$. Here, $\tau_{\mathbf{AC}}$, $\tau_{\mathbf{DB}}$, $\tau_{\mathbf{AD}}$, and $\tau_{\mathbf{BC}}$ are the travel time of each event, and they are corresponding to the propagation time and related path from point A to C, from point D to B, from point A to D, and from point B to C.

In seismic interferometry [34], the convolution of two traces in the time domain is equal to the multiplication of their respective Green's functions in the frequency domain, while cross correlation involves multiplying one trace with the complex conjugate of the other in the frequency domain. In the present scenario, the convolution of two seismic traces, $G(C, \tau_{\mathbf{AC}}|A)$ and $G(D, \tau_{\mathbf{DB}}|B)$, results in duplicated raypaths [as shown in Fig. 4(a)] between the subsurface points x and x'. To eliminate the duplicated raypath xx' as well as the two segments Ax and $x'D$, cross correlation is employed to the trace $G(D, \tau_{\mathbf{AD}}|A)$ with the result of the convolution, as shown in the following equation and Fig. 4(b):

$$\begin{aligned} G^{\text{vir}} &= G(C, \tau_{\text{AC}}|A)G(B, \tau_{\text{DB}}|D)G(D, \tau_{\text{AD}}|A)^* \\ &= e^{i\omega\tau_{\text{AC}}} \times e^{i\omega\tau_{\text{DB}}} \times e^{-i\omega\tau_{\text{AD}}} \\ &= e^{i\omega(\tau_{\text{AC}}+\tau_{\text{DB}}-\tau_{\text{AD}})} \\ &= e^{i\omega\tau_{\text{BC}}} \end{aligned} \tag{5}$$

where the variable ω is frequency, and the virtual wavefield $G^{\mathbf{vir}}$ has $\tau_{\mathbf{BC}}$ travel-time value, which is the same as the true wavefield $G_{\mathbf{BC}}$. The created virtual waveform is shown in Fig. 6(a), and the true and virtual waveform are indicated using blue and red lines. It can be observed that the virtual waveform exhibits a congruent phase with true trace; however, the amplitude spectrum demonstrates a notably sharper peak distribution. The reason is that there will be an extra amplitude spectrum $|W(\omega)|^2$, which is shown in Appendix A.

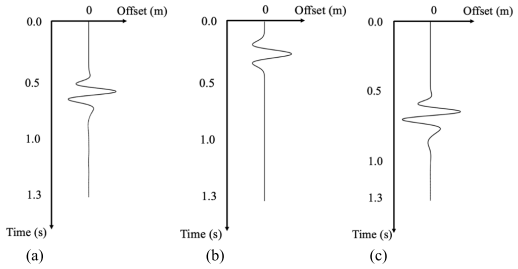

Fig. 5. Waveform related to (a) raypath AC, (b) raypath DB, and (c) raypath AD in Fig. 4(a).

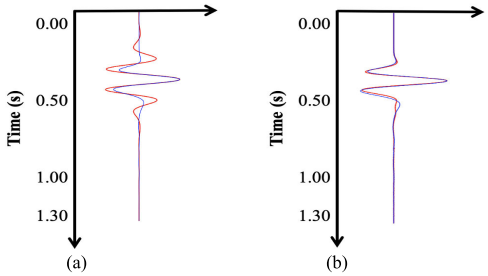

Fig. 6. Comparative analysis of virtual and true traces is conducted utilizing two distinct methodologies: (a) employing convolution and cross correlation techniques and (b) implementing source wavelet deconvolution to derive the virtual waveform. The virtual trace is represented by a red line, while the true trace is denoted by a black line.

C. Source Wavelet Deconvolution

One option to correct the dynamic character of virtual waveform is to employ source wavelet deconvolution [30], [36], which is to reduce the extra convolved source wavelet. Equation (6) provides the expression for the source wavelet deconvolution

$$\begin{aligned} D(B|C)^{\text{vir}} &= \frac{D^{\text{vir}}(B|C)}{D(A|D)D(A|D)^* + \epsilon} \\ &= \frac{e^{i\omega(\tau_{\text{AC}}+\tau_{\text{DB}}-\tau_{\text{AD}})}|W(\omega)|^2 W(\omega)}{e^{i\omega\tau_{\text{AD}}}e^{-i\omega\tau_{\text{AD}}}|W(\omega)|^2 + \epsilon} \\ &= W(\omega)e^{i\omega\tau_{\text{AD}}}. \end{aligned} \tag{6}$$

To prevent instability arising from small denominator value, we incorporate a small value ϵ at the corresponding location during the process. Fig. 6(b) shows the corrected waveform following deconvolution, which exhibits nearly identical dynamic characteristics as the true event. Although some discrepancies resulting from numerical errors may be observed, these are generally acceptable, as in practice, the waveform inversion misfit is influenced by numerous factors and cannot be reduced to zero. Therefore, any slight differences are often negligible and the virtual seismogram can still be effectively utilized in waveform inversion. The specific details are illustrated in Appendix B.

III. Numerical Example

A. Synthetic Model

In this section, we demonstrate the applicability of WPRI by applying it to a data set created using a synthetic velocity model. Fig. 7(a) presents the velocity model, which measures 1200 × 140 m and consists of two layers. The interface is located at a depth of 90 m, while the upper and lower layers have 500 and 4500 m/s, respectively. We have introduced a

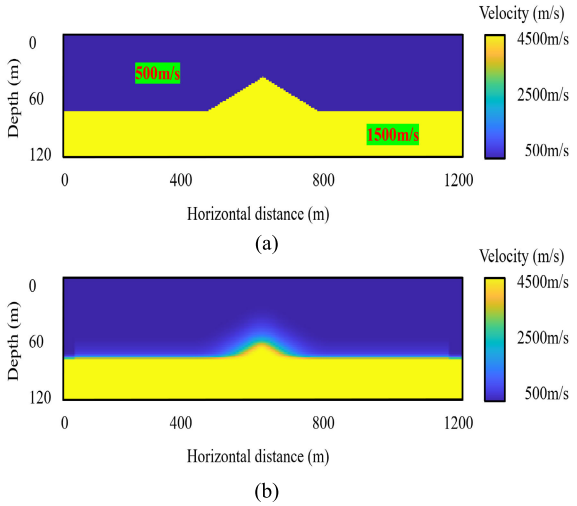

Fig. 7. (a) True velocity model used to create synthetic data. (b) Initial velocity used in EWI.

sharp horizontal velocity variation in the second layer, which violates the high-frequency assumption [37] to illustrate the feasibility of our waveform inversion procedure. The survey comprises a total of 90 sources and receiver points with 12-m spacing on the surface. To generate the seismograms, we utilized a fourth-order spatial and two-order time scheme finite-difference code [38] to simulate acoustic waveform with a total recording time of 0.8 s and a sample rate of 0.2 ms. At each source position, we applied a Ricker source wavelet with a peak frequency of 30 Hz.

Utilizing a total of 180 traces from the first and last CSGs, as well as select near-offset traces correlating to the direct waves, we have harnessed these inputs as the fundamental basis of our proposed WPRI technique. In order to eliminate the head wave presented in each of the selected traces, we applied a taper window spanning two to three wavelengths surrounding the first arrival travel time. The resulting muted the 1st and 90th shot gathers that were utilized in the calculation of the virtual waveform can be observed in Fig. 8(a) and (c), respectively. In addition, Fig. 8(b) shows the 20th shot gather containing solely near-offset traces. The muted data are converted to the frequency domain and are shown as combinations of multiplication and division related to convolution, cross correlation operations, and source wavelet deconvolution in the time domain that are applied to obtain the virtual event. Then, the seismic traces are transformed back into the time domain. Fig. 9(a) and (b) shows, respectively, the authentic synthetic and virtual 20th CSGs generated by means of the proposed WPRI technique. It is noteworthy that both shot gathers present identical travel-time details, pertaining to the kinematic nature of the signal. Furthermore, Fig. 9(c) presents a comparison of traces between 51 and 70 in the 20th genuine and virtual CSGs, where the former and latter are denoted by blue and red lines, respectively. We could see that virtual waveforms possess great resemblance to true waveforms. It demonstrates that our proposed WPRI technique can produce virtual waveforms with almost correct dynamic characters besides kinematic characters shown in Fig. 9(d) [24]. There are some Gibbs effects on virtual waveform because

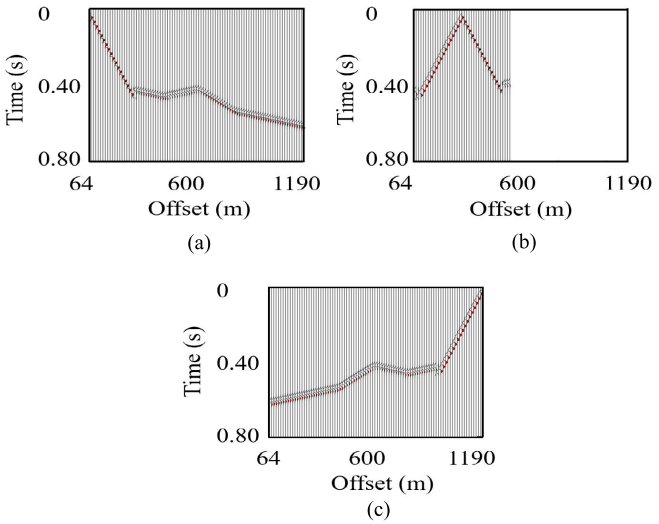

Fig. 8. (a) 1st, (b) 20th, and (c) 90th CSGs in the synthetic data generated by the velocity model shown in Fig. 7.

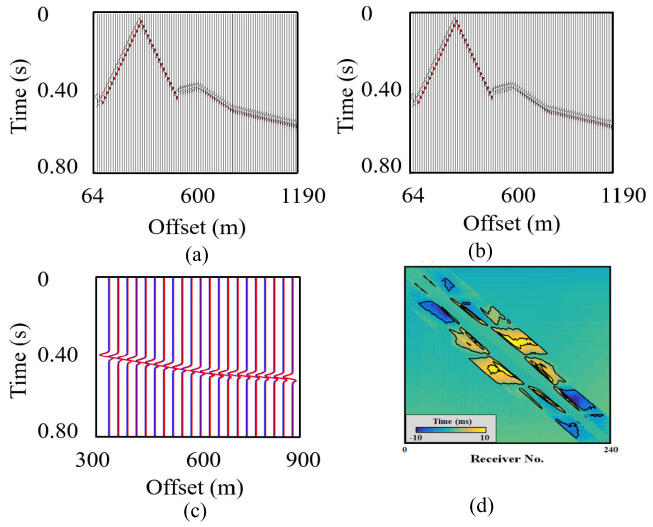

Fig. 9. 20th CSG of (a) true and (b) virtual CSGs. (c) Comparing traces 51–70 traces, blue lines are true traces, while red lines are virtual traces. (d) Travel-time difference between real and virtual travel times created by the travel-time PRI method [24].

we mute the seismic data and apply the convolution and cross correlation in the frequency domain [39], but these slight differences are not an important obstacle that prevents the use of these virtual traces in waveform inversion.

We first apply EWI and refraction wavefield migration on the true waveform. The initial model used for the EWI as shown in Fig. 7(b) is a smoothed version of the true model. The reconstructed velocity model of EWI is shown in Fig. 10(a), and it is noticeable that the inverted velocity model has strong agreement to the true velocity model. In addition, Fig. 10(b) represents the refraction wavefield migration image, which utilizes interferometry to create virtual reflection shot gather from refraction wavefield and prestack depth migration (PSDM) to construct subsurface reflectivity of refractor [20]. In this case, we use Kirchhoff PSDM to map interferometric reflection gathers to map the refractor location. We notice that the sparsity of seismic survey will lead to the linear artifacts above the refractor, as shown in Fig. 7(b). The WPRI's virtual data shown in Fig. 9(b) are, now, used for EWI and refraction

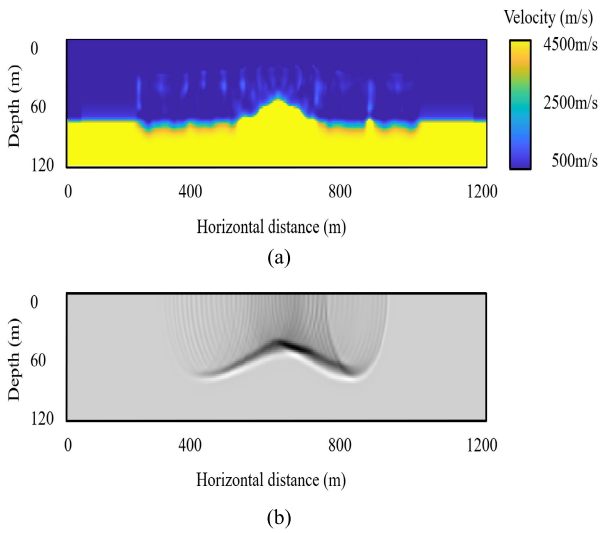

Fig. 10. (a) EWI velocity tomogram and (b) refraction wavefield migration result of true dataset.

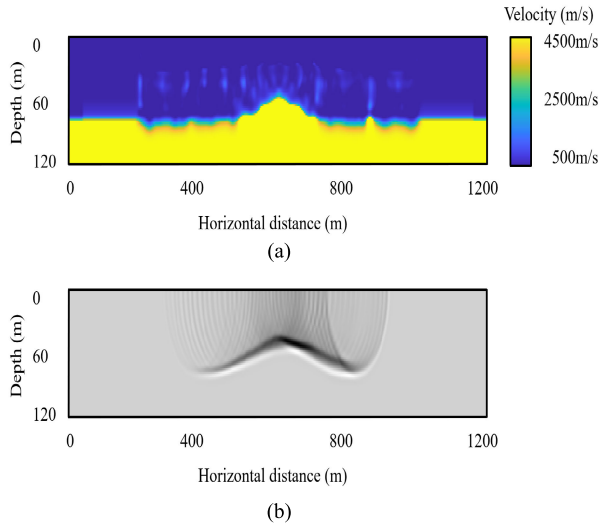

Fig. 11. (a) EWI velocity tomogram and (b) refraction wavefield migration result of virtual dataset created by WPRI.

wavefield migration. The final tomography and imaging results are shown in Fig. 11(a) and (b) and reveal the correct velocity distribution although there are some linear artifacts due to the sparsity of seismic survey. In addition, they have strong correspondence to the true velocity model and imaging results of virtual data in Fig. 10(a) and (b). Fig. 12(a) and (b) represents the difference value distribution of EWI and refraction wavefield migration result in this synthetic numerical example. The comparison shows that the value difference of most pixels is very small. It demonstrates that virtual data created by our advocated WPRI technique can produce velocity models and reflectivity that are close to the seismic imaging results of the true dataset.

B. Field Data

A seismic survey recorded near the Gulf of Aqaba in Saudi Arabia (see Fig. 13) [40] is also used here to illustrate our method's feasibility. This site is selected because the geological background of the site [40] shows several new fault ruptures, which cause subsurface geological discontinuity. The

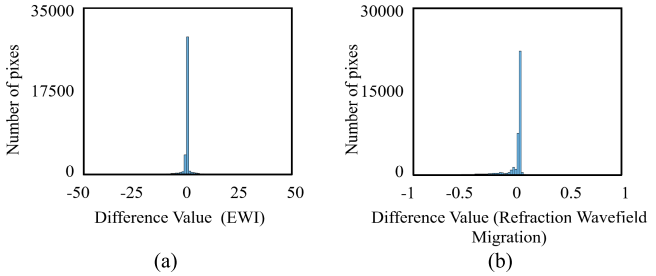

Fig. 12. Distribution of difference value of (a) EWI and (b) refraction wavefield migration result using true and virtual dataset in synthetic numerical example.

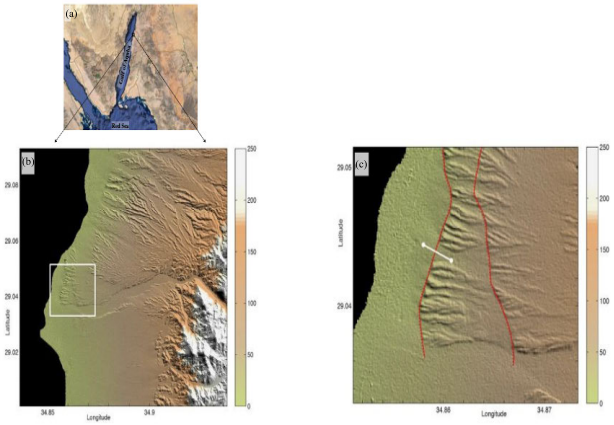

Fig. 13. (a) Google Earth satellite image showing the location of the study area at the eastern side of Gulf of Aqaba. (b) Shaded relief topographic map of the study area (color scale in meters), with details shown in (c), including the seismic profile (white) and two easily identified normal faults (red). Cited from [40].

recorded 2-D profile is 300 m long and placed at an alluvial fault location. A total of 120 receivers with 2.5-m spacing are deployed and one shot is fired next to each receiver. In addition, a 200-lb accelerated weightdrop is used to generate the seismic energy. The signal-to-noise ratio (SNR) of this dataset is very high, as shown in Fig. 14(a). To eliminate any high-frequency noises, we apply a bandpass filter from 10 to 40 Hz on this set of data and the result is shown in Fig. 14(b). To mute around the early arrival waveform, a taper window with three periods is applied on the recorded dataset and the result is shown in Fig. 14(c). The proposed WPRI technique is applied on a pair of reciprocal shot gathers located at the two sides of the survey (240 traces) to generate the virtual traces of all other 118 shot gathers (a total of 14 000 virtual traces). Similar to the synthetic example, we used a couple of infilled shot gathers where only traces with direct wave are kept to interpolate for direct-wave information, as shown in Fig. 15(a) and (b).

Guided waves are clearly seen below the refraction wavefield in this field example. The virtual 20th CSG generated by the proposed WPRI methodology is represented in Fig. 15(b). We could see that the refraction wavefield has been recovered successfully. In addition, other wave modes around the refraction wavefield such as the guided wave can be eliminated since this type of wave mode does not conform to the refraction wavefield physical path propagation, which is the basis of WPRI. The comparison between true and virtual traces in the offset range of 210–225 m (corresponding to

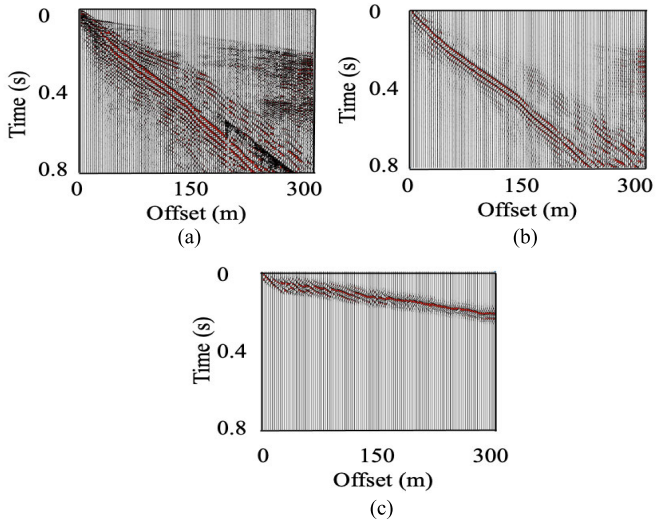

Fig. 14. 1st CSG in (a) original, (b) filtered, and (c) muted Aqaba Gulf data.

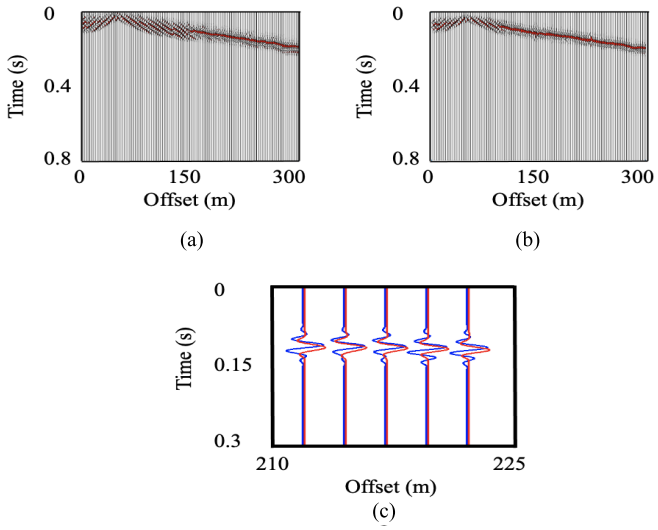

Fig. 15. Muted 20th CSG of (a) filtered Aqaba Gulf data and (b) virtual data created using WPRI technology. (c) Comparison between true (blue) and virtual (red) of the 86th-to-90th traces.

traces 86–90) is shown in Fig. 15(c), and they have similar kinematic and dynamic characters. In this field data example, the feasibility of WPRI approach to recover both kinematic and dynamic characters has been demonstrated. We applied EWI and migration on true and virtual datasets. As shown in Fig. 16(a), the initial velocity model used for both of these two methods is constructed by travel-time tomography [17]. It is obvious that the fault is located at the midpoint of the model, which is close to the geological survey result. The reflectivity constructed by refraction wavefield migration is shown in Fig. 16(b).

The tomogram created by EWI data is shown in Fig. 17(a), and it could reveal some small anomalies and indicate fault successfully. As shown in Fig. 17(b), the refraction wavefield migration image using the velocity model constructed by EWI has a superior degree compared to Fig. 16(b) due to the improvement of background velocity model. Fig. 18(a) and (b) shows EWI and refraction wavefield migration results of virtual dataset, which has a great resemblance to the results of true data, respectively. Fig. 19(a) and (b) shows the

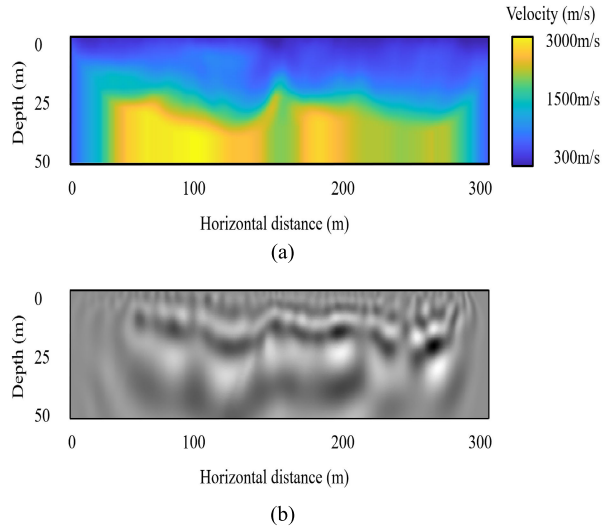

Fig. 16. (a) Travel-time tomogram of Aqaba dataset. (b) Refraction wavefield migration calculated from travel-time tomogram and Aqaba Gulf dataset.

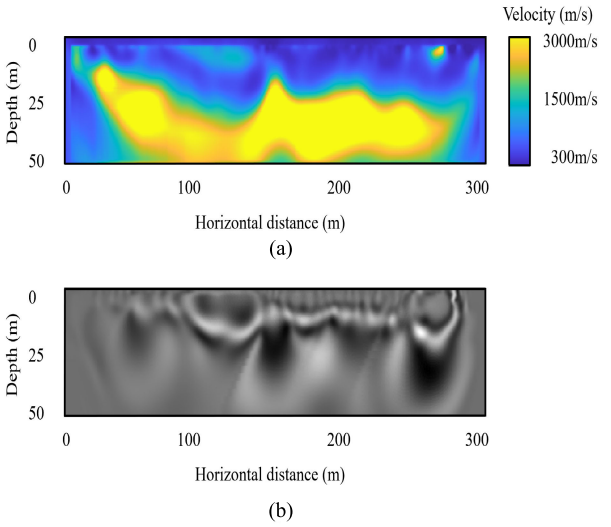

Fig. 17. (a) EWI tomogram of true Aqaba dataset. (b) Refraction wavefield migration calculated from EWI tomogram and Aqaba dataset.

discrepancy distribution of EWI and refraction wavefield migration values between the true and virtual datasets, respectively. The vast majority of pixels exhibit negligible value differences. Hence, the present field data example effectively validates the viability and practicality of our methodology in the context of real data analysis.

IV. Discussion

A. Field Data Noises' Effect

Data noises caused by different environmental factors in real data examples are expected. This type of problem may lead to the failure of WPRI method. Here, we discuss a simple numerical model consisting of a flat interface (see Fig. 20) to illustrate the data noises' effect. This model has two layers, and the P-wave velocity of the first and second layers is 500 and 4500 m/s, respectively. The thickness of the first layer is 80 m. A total of 90 sources and 90 receivers are placed at the surface with 12-m spacing between each of the two sources/receivers. To generate the seismic data,

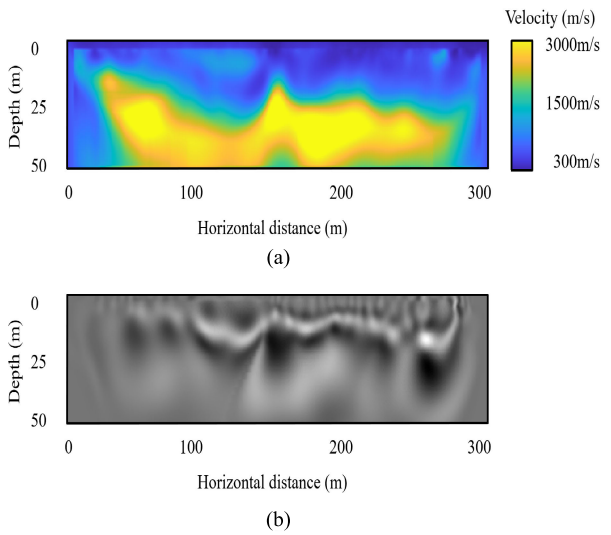

Fig. 18. (a) EWI tomogram of the WPRI-virtual Aqaba dataset. (b) Refraction wavefield migration calculated from WPRI-EWI tomogram and Aqaba dataset.

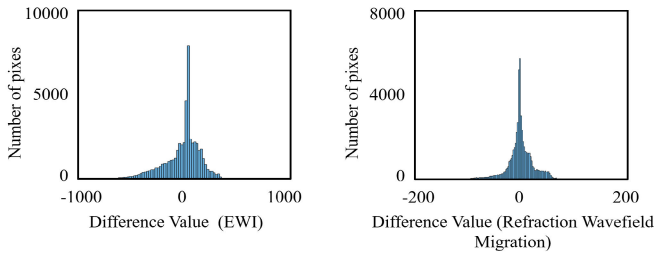

Fig. 19. Distribution of difference value of (a) EWI and (b) refraction wavefield migration result using true and virtual dataset in Aqaba field dataset.

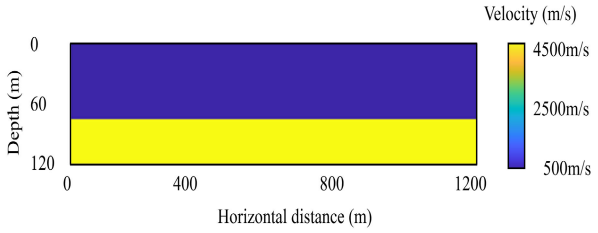

Fig. 20. Synthetic velocity model used to test noise effect.

a Ricker wavelet with 30-Hz middle frequency is activated and the generated wavefield is calculated for each source location using a 0.2-ms time step.

We add noises to the generated data, which will lead to kinematic and dynamic uncertainty, and hence, the seismic data will not conform the far-field reciprocity theorem. The procedure to add noises is shown as follows.

1) Generate a series of random variables.
2) Use this set of random variables to obtain the corresponding time shift values.
3) Apply these time shift values on each trace of seismic data to create kinematic uncertainty.
4) Add random noises on each trace for dynamic uncertainty.

After muting early arrival waveform, the 1st, 20th, and 90th CSG of the noisy data are shown in Fig. 21(a)–(c), respectively. We could see that the muted noisy seismograms do not obey the reciprocity theorem. We utilize the 1st and 90th CSG as the input information of WPRI procedure, and Fig. 21(d)

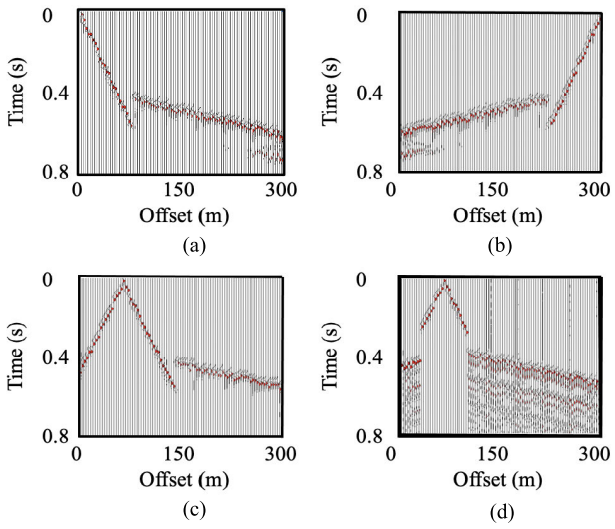

Fig. 21. (a) 1st, (b) 90th, and (c) 20th CSG in the muted noisy seismic data. (d) 20th CSG in the virtual seismogram generated by WPRI.

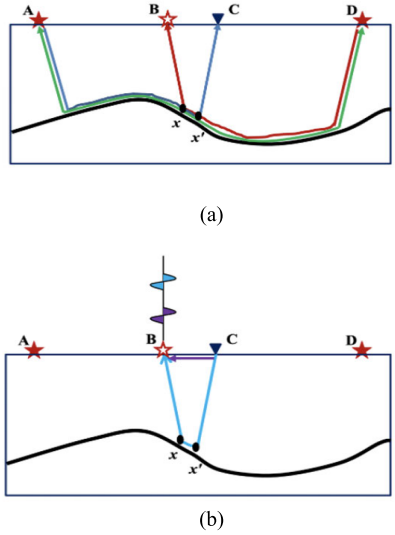

Fig. 22. Sketch shows the WPRI method for a two-layer model, where the lower layer has a faster seismic velocity than the upper layer. (a) Green line represents the propagation direction associated with the wavefield activated at A and received at *D*. The blue line indicates the wavefield from A to C. The red line is the wavefield from D to B. (b) Blue line represents the virtual PRI raypath from B to C calculated by convolution and cross correlation operations. The trace above the model represents the virtual trace from a virtual source at B and received at C.

shows the generated virtual 20th CSG. By comparison with the true noisy 20th CSG in Fig. 21, it is evident that the recovered seismogram does not have good quality and cannot be used in seismic imaging methods.

B. Application Limitation of WPRI

As shown in Fig. 22(a), for near-offset source and receiver pairs, the head wave associated with the direct-wave mode does not adhere to the wavepath of the virtual wavefield used in (5). Fig. 22(b) shows the real near-offset waveform, which is denoted by the purple arrow. They diverge from the virtual wavefield calculated through our approach represented by the blue dashed curve. In such scenarios, it is necessary to gather additional short offset traces and perform interpolation prior to applying the WPRI technology. Furthermore, for some cases

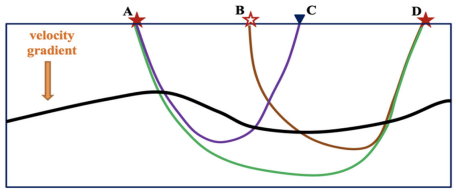

Fig. 23. WPRI method for a two-layer model, where the lower layer has a faster seismic velocity than the upper layer and there is a strong velocity gradient in the second layer. The green line is the propagation direction associated with the wavefield activated at A and received at D. The purple line indicates the wavefield from A to C. The brown one is the wavefield from D to B. There is no common path between the propagation path between these three wave modes.

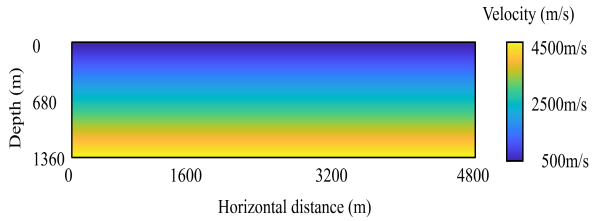

Fig. 24. Synthetic velocity model used to test WPRI in case of a strong velocity gradient.

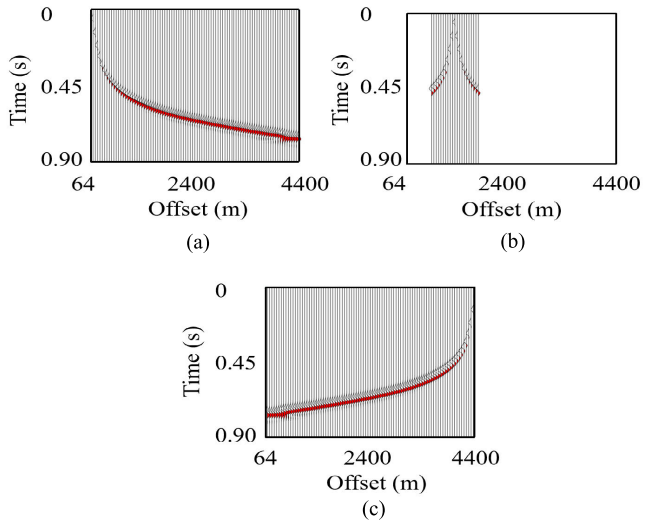

Fig. 25. (a) 1st, (b) 20th, and (c) 90th CSGs in the synthetic data of the velocity model in Fig. 24.

involving far-offset traces and gradient velocity models, the diving wave is frequently encountered so that the wavefield from B to C cannot be derived by canceling the common wavepath, as shown in Fig. 23. Another reason is that the sources are not at stationary positions in the case of diving waves. Thus, the WPRI methodology cannot be used to obtain virtual waveform in the model with strong velocity gradient.

As an example, the velocity model shown in Fig. 24 is used to illustrate this limitation. The size of this model is 4800 and 1360 m. The model shows a strong gradient velocity value ranging from 500 to 4500 m/s. There are 90 sources and 90 geophones along the surface with spacing equal to 48 m. The source wavelet is a Ricker wavelet with a 10-Hz peak frequency. In addition, we have 9001 time steps with 0.1 ms. The forward simulation methodology is fourth-space and second-time order finite-difference algorithm of acoustic wave equation. The first and last CSGs which we used as input to the WPRI are shown in Fig. 25(a) and (b), respectively.

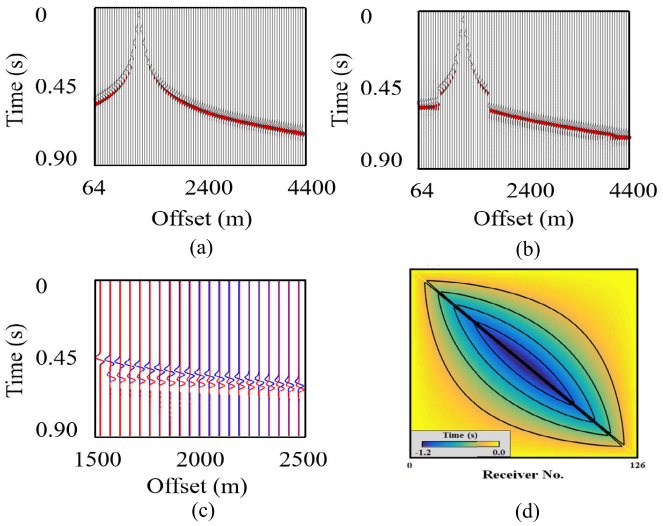

Fig. 26. (a) Real and (b) virtual CSG no. 20. The real traces show a clear curvature in the refraction event due to the strong velocity gradient (Fig. 24), while the virtual traces lost this curvature. (c) Comparison between the real and WPRI-virtual traces. (d) Travel-time difference between real and PRI-virtual travel times in case of strong velocity gradient as discussed in [24].

We also kept several near-offset traces related to direct wave, and Fig. 25(c) shows the 20th CSG as an example. The seismograms that are shown in Fig. 26(a) and (b) are the real and virtual 20th CSGs in our technology. A shift between the raw and virtual traces at the transition zone between direct and diving waves is clearly observed; in addition, the virtual traces lost the curvature shown on the real traces [Fig. 26(a)]. Here, this curvature is due to the strong velocity gradient; however, the virtual traces show a constant slop with no curvature [see Fig. 26(b)]. Fig. 26(c) shows the comparison between the real and virtual traces in the case of strong gradient velocity model, which highlights the absence of the curvature in the virtual traces. This observation is in accordance with the failure case of travel-time PRI for gradient velocity model discussed in [24], see Fig. 26(d). This is true, also for far-offset traces, where real and virtual seismograms have different dynamic characters. This example suggests that our proposed WPRI method is not applicable in the case of strong diving wave examples.

V. Conclusion

Based on the seismic interferometry principle, we extend the scope of travel-time PRI to the waveform domain in which numerous refraction wavefields can be calculated and utilize wavelet deconvolution to correct dynamic character. Our methodology could obtain virtual waveform with less acquisition cost in 2-D acquisition geometries used often in the petroleum industry and engineering. Each trace, which is not recorded directly, can be calculated from the first, the last shot gathers, and several infilled short offset gathers, but the diving waves that are associated with gradient velocity models cannot be derived using this method. The virtual data created by our proposed method could be used in waveform-based inversion and refraction wavefield migration to image the subsurface structure. In the future, we will investigate WPRI applicability in more complex geological structures and its extension in other wave modes.

Appendix A

The recorded seismogram can be presented by the convolution of source wavelet and Green function. In the frequency domain, the recorded data related to raypaths AC, BD, and AD can be presented as follows:

$$\begin{aligned} D(A|C) &= W(\omega)G(A|C) \\ D(B|D) &= W(\omega)G(B|D) \\ D(A|D) &= W(\omega)G(A|D). \end{aligned} \tag{A-1}$$

In the WPRI procedure, we need to calculate the convolution of $D(A|C)$ and $d(D|B)$ first. We refer the convolution of $D(A|C)$ and $D(D|B)$ to as D_1 in the frequency domain and can be presented as follows:

$$\begin{aligned} D_1 &= D(A|C)D(B|D) \\ &= W(\omega)G(A|C)W(\omega)G(B|D) \\ &= W(\omega)^2G(A|C)G(B|D). \end{aligned} \tag{A-2}$$

Then, we should estimate the cross correlation of the convolution result D_1 and $D(D|B)$, and this step is equal to the multiplication of D_1 and $D(A|D)$'s conjugate term. The conjugate of $D(A|D)$ is presented as follows:

$$D(A|D)^* = W(\omega)^*G(A|D)^*. \tag{A-3}$$

We use D_2 to represent the cross correlation result, and the corresponding step can be shown as follows:

$$\begin{aligned} D_2 &= D_1D(A|D)^* \\ &= W(\omega)^2G(A|C)G(B|D)W(\omega)^*G(A|D)^* \\ &= W(\omega)W(\omega)^*W(\omega)G(A|C)G(B|D)G(A|D)^* \\ &= |W(\omega)|^2W(\omega)G(B|C) \end{aligned} \tag{A-4}$$

where $G(A|C)G(B|D)G(A|D)^* = G(B|C)$ is demonstrated in Section II. It is obvious that there is an extra amplitude spectrum $|W(\omega)|^2$ contained in the WPRI result D_2.

Appendix B

For the extra convolved source wavelet, we divide the result calculated by convolution and cross correlation over $|W(\omega)|^2$ in the frequency domain to remove this extra term and the result is displayed using D_3 as follows:

$$\begin{aligned} D_3 &= \frac{D_2}{|W(\omega)|^2} \\ &= \frac{|W(\omega)|^2W(\omega)G(B|C)}{|W(\omega)|^2} \\ &= W(\omega)G(B|C). \end{aligned} \tag{B-1}$$

References

[1] X. Zhu, D. P. Sixta, and B. G. Angstman, "Tomostatics: Turning-ray tomography + static corrections," *Lead. Edge*, vol. 11, no. 12, pp. 15–23, 1992.

[2] H. Yu, S. Hanafy, and L. Liu, "A weighted closure-phase statics correction method: Synthetic and field data example," *IEEE Trans. Geosci. Remote Sens.*, vol. 60, 2022, Art. no. 5913713.

[3] C. A. Zelt and P. J. Barton, "Three-dimensional seismic refraction tomography: A comparison of two methods applied to data from the Faeroe basin," *J. Geophys. Res., Solid Earth*, vol. 103, no. B4, pp. 7187–7210, Apr. 1998.

[4] J. Zhang, "Nonlinear refraction and reflection traveltime tomography," Ph.D. thesis, Dept. Earth, Atmos., Planet. Sci., Massachusetts Inst. Technol., Cambridge, MA, USA, 1997.
[5] J. Zhang and M. Toksöz, "Nonlinear refraction traveltime tomography," *Geophysics*, vol. 63, no. 5, pp. 1496–1823, 1998.
[6] S. Stein and M. Wyession, *An Introduction to Seismology, Earthquakes, and Earth Structure*. Hoboken, NJ, USA: Blackwell, 2003.
[7] W. Jiang and J. Zhang, "First-arrival traveltime tomography with modified total-variation regularization," *Geophys. Prospecting*, vol. 65, no. 5, pp. 1138–1154, 2017.
[8] J. Zhang and M. Toksöz, "Joint refraction traveltime migration and tomography," in *Proc. SAGEEP, Environ. Eng. Geophys. Soc.*, 1997, pp. 901–910.
[9] Y. Wang and J. Zhang, "Joint refraction traveltime tomography and migration for multilayer near-surface imaging," *Geophysics*, vol. 84, no. 6, pp. U31–U43, Nov. 2019.
[10] S.-H. Hung, F. A. Dahlen, and G. Nolet, "Wavefront healing: A banana–doughnut perspective," *Geophys. J. Int.*, vol. 146, no. 2, pp. 289–312, Aug. 2001.
[11] P. R. Williamson and M. H. Worthington, "Resolution limits in ray tomography due to wave behavior: Numerical experiments," *Geophysics*, vol. 58, no. 5, pp. 616–777, 1993.
[12] J. Spetzler and R. Snieder, "The effect of small scale heterogeneity on the arrival time of waves," *Geophys. J. Int.*, vol. 145, no. 3, pp. 786–796, Jun. 2001.
[13] A. Tarantola, "Inversion of seismic reflection data in the acoustic approximation," *Geophysics*, vol. 49, no. 8, pp. 1259–1266, 1984.
[14] P. Mora, "Elastic wavefield inversion," Ph.D. thesis, Dept. Geophys., Stanford Univ., Stanford, CA, USA, Sep. 1987.
[15] J. Virieux and S. Operto, "An overview of full-waveform inversion in exploration geophysics," *Geophysics*, vol. 74, no. 6, pp. WCC1–WCC26, Nov. 2009.
[16] O. Gauthier, J. Virieux, and A. Tarantola, "Two-dimensional nonlinear inversion of seismic waveforms: Numerical results," *Geophysics*, vol. 51, no. 7, pp. 1387–1403, Jul. 1986.
[17] J. Sheng, A. Leeds, M. Buddensiek, and G. T. Schuster, "Early arrival waveform tomography on near-surface refraction data," *Geophysics*, vol. 71, no. 4, pp. U47–U57, Jul. 2006.
[18] R. G. Pratt, Z.-M. Song, P. Williamson, and M. Warner, "Two-dimensional velocity models from wide-angle seismic data by wavefield inversion," *Geophys. J. Int.*, vol. 124, no. 2, pp. 323–340, Feb. 1996.
[19] Y. Luo and G. Schuster, "Wave-equation traveltime inversion," *Geophysics*, vol. 56, no. 5, pp. 645–653, 1991.
[20] Y. Shen and J. Zhang, "Refraction wavefield migration," *Geophysics*, vol. 85, no. 6, pp. Q27–Q37, Nov. 2020.
[21] D. Draganov, K. Wapenaar, and J. Thorbecke, "Seismic interferometry: Reconstructing the Earth's reflection response," *Geophysics*, vol. 71, no. 4, pp. SI61–SI70, Jul. 2006.
[22] G. T. Schuster, J. Yu, J. Sheng, and J. Rickett, "Interferometric/daylight seismic imaging," *Geophys. J. Int.*, vol. 157, no. 2, pp. 838–852, May 2004.
[23] B. Hornby and J. Yu, "Interferometric imaging of a salt flank using walkaway VSP data," *Lead. Edge*, vol. 26, no. 6, pp. 673–800, 2007.
[24] S. Hanafy and G. T. Schuster, "Parsimonious refraction interferometry and tomography," *Geophys. J. Int.*, vol. 209, no. 2, pp. 695–712, May 2017.
[25] L. Fu, S. M. Hanafy, and G. T. Schuster, "Parsimonious wave-equation travel-time inversion for refraction waves," *Geophys. Prospecting*, vol. 65, no. 6, pp. 1452–1461, Nov. 2017.
[26] S. Hanafy, J. Li, and G. Schuster, "Time lapse parsimonious refraction interferometry: A field experiment," SEG Tech. Program Expanded Abstr., Aug. 2018, doi: 10.1190/segam2018-2986382.1.
[27] S. M. Hanafy, H. Hoteit, J. Li, and G. T. Schuster, "Near-surface real-time seismic imaging using parsimonious interferometry," *Sci. Rep.*, vol. 11, no. 1, pp. 1–9, Mar. 2021.
[28] J. Li, S. Hanafy, and G. T. Schuster, "Parsimonious surface wave interferometry," *Geophys. J. Int.*, vol. 212, no. 3, pp. 1536–1545, Mar. 2018.
[29] N. Bleistein, "On the imaging of reflectors in the Earth," *Geophysics*, vol. 52, no. 7, pp. 931–942, Jul. 1987.
[30] R. Snieder, "Extracting the building response using seismic interferometry: Theory and application to the Millikan library in Pasadena, California," *Bull. Seismological Soc. Amer.*, vol. 96, no. 2, pp. 586–598, Apr. 2006.
[31] K. Wapenaar and J. Fokkema, "Green's function representations for seismic interferometry," *Geophysics*, vol. 71, no. 4, pp. SI33–SI46, 2006.
[32] O. Al-Hagan, S. M. Hanafy, and G. T. Schuster, "Iterative supervirtual refraction interferometry," *Geophysics*, vol. 79, no. 3, pp. Q21–Q30, May 2014.
[33] X. Duan and J. Zhang, "Multitrace first-break picking using an integrated seismic and machine learning method," *Geophysics*, vol. 85, no. 4, pp. WA269–WA277, Jul. 2020.
[34] G. T. Schuster, *Seismic Interferometry*. Cambridge, U.K.: Cambridge Univ. Press, 2009.
[35] P. Morse and H. Feshbach, *Methods of Theorical Physics (Part 1)*. New York, NY, USA: McGraw-Hill, 1953.
[36] I. Vasconcelos and R. Snieder, "Interferometry by deconvolution: Part 1—Theory for acoustic waves and numerical examples," *Geophysics*, vol. 73, no. 3, pp. S115–S128, 2008.
[37] N. J. Bleistein, J. K. Cohen, and J. W. Stockwell, *Mathematics of Multi-Dimensional Seismic Imaging, Migration, and Inversion*. New York, NY, USA: SpringerVerlag, 2001.
[38] A. R. Levander, "Fourth-order finite-difference P-SV seismograms," *Geophysics*, vol. 53, no. 11, pp. 1425–1436, Nov. 1988.
[39] O. Yilmaz, *Seismic Data Analysis*. Thousand Oaks, CA, USA: SEG Publising, 2001.
[40] S. Hanafy, J. Sigurjon, and K. Yann, "Imaging normal faults in alluvial fans using geophysical techniques: Field example from the coast of Gulf of Aqaba, Saudi Arabia," *SEG Tech. Program Expanded Abstr.*, pp. 1–6, Oct. 2014.

Yicheng Zhou (Student Member, IEEE) received the bachelor's degree in applied geophysics from Jilin University, Changchun, China, in 2015, and the master's degree in theoretical geophysics from the University of Science and Technology of China, Hefei, China, in 2018. He is currently pursuing the Ph.D. degree in applied geophysics with the King Fahd University of Petroleum and Mineral (KFUPM), Dhahran, Saudi Arabia.

After his master's degree, he worked at the Southern University of Science and Technology (SUSTech), Shenzhen, China; the King Abdullah University of Science and Technology (KAUST), Thuwal, Saudi Arabia; and the Peng Cheng Laboratory, Shenzhen, for three years. His research interests include seismic imaging, machine learning, and microseismic geophysics.

Sherif M. Hanafy received the B.Sc. and M.Sc. degrees from Cairo University, Giza, Egypt, in 1993 and 1996, respectively, and the Ph.D. degree in geophysics from Kiel University, Kiel, Germany, in 2002.

He was a Senior Research Scientist at the King Abdullah University of Science and Technology, Thuwal, Saudi Arabia, from 2009 to 2018; a Post-Doctoral Fellow and an Adjunct Associate Professor at The University of Utah, Salt Lake City, UT, USA, from 2004 to 2007; and an Assistant Professor at Cairo University, Giza, Egypt, from 2002 to 2009. He is currently an Associate Professor of geophysics with the King Fahd University of Petroleum and Mineral, Dhahran, Saudi Arabia. He has more than 25 years of experience in academia and 12 years of cooperation with industry as a member of the Utah Tomography and Modeling/Migration (UTAM) and Center for Subsurface Imaging and Fluid Modeling (CSIM) consortiums. During this time period, he has coauthored more than 50 articles in peer-reviewed journals and more than 70 expanded abstracts at international conferences. His research interests include geophysical field methods, seismic interferometry, travel-time tomography, early arrival tomography, seismic modeling, seismic inversion and migration, data interpolation/extrapolation, shallow applications of resistivity and ground penetrating radar (GPR) methods, and, recently, machine learning.

Dr. Hanafy received the Ph.D. Scholarship from Deutscher Akademischer Austauschdienst (DAAD), Germany, in 1999, and the Fulbright Fellowship in 2004 to pursue post-doctoral studies at The University of Utah.